



The Society shall not be responsible for statements or opinions advanced in papers or discussion at meetings of the Society or of its Divisions or Sections, or printed in its publications. Discussion is printed only if the paper is published in an ASME Journal. Authorization to photocopy material for internal or personal use under circumstance not falling within the fair use provisions of the Copyright Act is granted by ASME to libraries and other users registered with the Copyright Clearance Center (CCC) Transactional Reporting Service provided that the base fee of \$0.30 per page is paid directly to the CCC, 27 Congress Street, Salem MA 01970. Requests for special permission or bulk reproduction should be addressed to the ASME Technical Publishing Department.

Aerodynamics of a Centrifugal Compressor Impeller with Transonic Inlet Conditions

H. Krain

B. Hoffmann

H. Pak

German Aerospace Research Establishment

Institute for Propulsion Technology

Linder Höhe 51147 Köln, Germany

Abstract

Performance and laser measurement results are presented for a transonic centrifugal compressor stage, equipped with a backswept rotor designed for 586 m/s tip speed and a mean relative inlet tip Mach number of 1.30.

The flow field features of the rotor are analysed in detail with the help of laser measurements and the results obtained from a 3D viscous calculation. Both laser measurements and calculations are carried out for the impeller's design point and a comparison between measured and calculated data is presented for four measurement planes representing the inlet, exit and channel flow conditions. The maximum relative Mach number is found to be 1.45 and a jet/wake type flow exists in the rear part of the flow channel with the wake concentrating in the shroud region. For the operating point investigated, the wake development is due more to the strong shroud curvature in the meridional plane than to a shock induced boundary layer separation. Laser measurements and calculations point to a significant flow displacement in the impeller exit region caused by the wake flow. The theoretical results indicate that a flow separation occurs also at the front side of the vaneless diffuser.

Nomenclature

List of Symbols

| | |
|-----------|---|
| b | Channel height from shroud to hub (Fig. 9) |
| c | Absolute Velocity [m/s] |
| c_m | Meridional velocity component [m/s] |
| c_u | Absolute circumferential velocity component [m/s] |
| k | Turbulent energy |
| M_{rel} | Relative Mach number |

| | |
|---------------|--|
| \dot{m} | Mass flow rate [Kg/s] |
| m/m_{ges} | Relative shroud length referred to impeller shroud |
| N_s | Specific speed [Balje's dimensions] |
| n | Shaft speed [rpm] |
| p | Pressure [N/m ²] |
| r | Radius |
| T | Temperature [K] |
| v_x | Velocity component parallel to machine axis |
| v_t | Velocity component perpendicular to meridional plane |
| v_r | Velocity component perpendicular to v_x, v_t |
| u_2 | Rotor tip speed [m/s] |
| w | Relative velocity [m/s] |
| y^+ | Wall distance |
| z | Distance from shroud (Fig. 9) |
| β | Relative flow angle (from tangential) |
| ε | Turbulent dissipation |
| η_{pt12} | Total/total polytropic efficiency |
| η_{stt} | Total/total isentropic efficiency |
| π_{t12} | Total pressure ratio of rotor |
| ρ | Density [kg/m ³] |
| ρ_h | Degree of reaction |
| Φ_2 | Throughflow coefficient c_{m2}/u_2 |

Subscripts

| | |
|-----|------------------------|
| 1 | Rotor inlet |
| 2 | Rotor exit |
| 3 | Diffuser inlet |
| 4 | Diffuser exit |
| 1t | Tip rotor leading edge |
| t | Total |
| tt | Total/total |
| red | Corrected |

Introduction

The requirements for low cost, low weight and small size often force designers of centrifugal compressors to design for very compact machines despite the need to maintain efficiency levels.

In principle, the steps to meet these requirements are clear:

- An increase of the compressor's specific speed results in a reduction of the rotor exit diameter and thus in a weight and size reduction of the stage.
- An increase of the stage pressure ratio may reduce the number of stages and can thus result in a further reduction of the machine's weight and size.

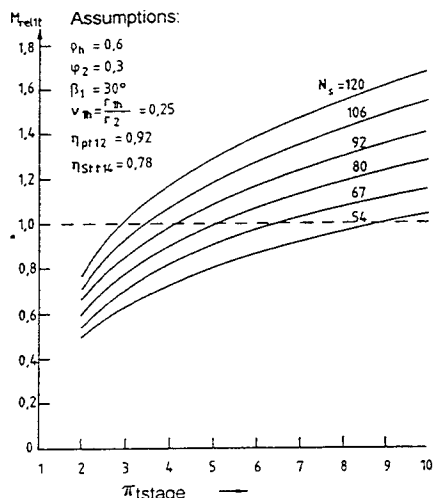


Fig. 1 Relative Mach number at the tip of the rotor leading edge, flow without inlet swirl.

But both steps increase the Mach number level of the flow inside the machine. Figure 1 illustrates this effect for a compressor which has 34 deg. backsweep from the radial. Here, the mean relative Mach number at the tip of the rotor leading edge has been plotted against stage pressure ratio with specific speed as a parameter. For stage pressure ratios of about 3 and specific speed of $N_s=120$ such compressors already operate with transonic rotor inlet flow. The pressure ratio that gives transonic flow is even lower when backsweep is higher than assumed here. Therefore, many compressors with rather moderate pressure ratios operate with transonic inlet conditions and the majority of advanced compressors using backswept rotors and having pressure ratios greater than 3 can be supposed to have transonic rotor flow too. Often the transonic flow conditions are simultaneously present in the diffuser inlet region. Centrifugal compressors with high flow Mach number levels are also known very often to have low efficiencies (Rodgers, 1991) which may be due to the widely unknown impact of shocks and shock/boundary layer interactions on rotor and diffuser flow. The aim of this paper is to contribute to a clarification of these phenomena by presenting measured and calculated results for a rotor having a mean relative inlet tip Mach number of 1.30.

Many high quality laser and hot wire measurement data are available for centrifugal rotors with subsonic flow (Pinarbasi and Johnson, 1994, Hathaway et al., 1992, Chriss et al., 1994, Ubaldi et al., 1994, Josuhn, 1994,

Eckardt, 1976, Casey et al., 1990, Krain, 1981, Krain and Hoffmann, 1989 a). These data are used by designers and scientists to check their design philosophy and/or to validate their CFD codes (Casey et al., 1990, Dalbert et al., 1993, Howard et al., 1994, Moore and Moore, 1990, Dawes, 1994, Hah and Krain, 1990). But only a few detailed experimental data have been published for high pressure ratio centrifugal compressors running with transonic rotor and/or diffuser inlet flow (Pak, Krain and Hoffmann, 1992, Colantuoni and Colella, 1992). This seems to be due to the rather difficult measurement conditions occurring at the rotor inlet and exit. Especially in the rotor exit region small dimensions, high temperatures, high velocities and highly fluctuating flow in the absolute frame make it difficult to resolve the flow field.

A DLR test rig, especially designed for testing high specific speed, high pressure ratio compressors was used for taking the measurement data to be presented in this paper. The available conventional DLR measurement technique and the laser velocimetry developed by Schodl (1989) were applied. In parallel, 3D calculations were carried out that contributed to a deeper insight into the flow physics of the tested rotor, primarily in those areas where measurements could not be taken.

Test Compressor and Measurement Technique

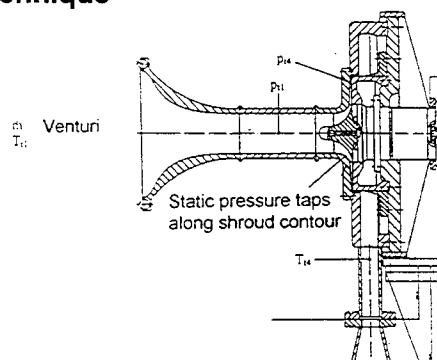


Fig. 2 Cross section of research compressor

Figure 2 shows a cross section of the centrifugal compressor stage used for the experimental and theoretical investigations. The main elements are the high specific speed ($N_s=105$) backswept rotor and the vaneless constant area diffuser. This diffuser ensures a wide flow range and is only applied for the initial tests that mainly deal with rotor flow. Typically, compressors of this kind are equipped with vaned diffusers having higher pressure recovery than vaneless diffusers (Japikse, 1992, Yoshinaka, 1994, Rodgers, 1982, Simon et al., 1986, Eisenlohr and Chladek, 1993). The vaneless diffuser will be replaced by a vaned type diffuser when the studies are extended to the whole stage.

Table 1 : Impeller design data

| | | |
|-------------------------|------------------|------|
| Shaft speed | $n = 50000$ | rpm |
| Mass flow rate | $\dot{m} = 2.55$ | Kg/s |
| Specific speed | $N_s = 105$ | |
| Blade number | $Z_R = 13+13$ | |
| Leading edge hub radius | $r_{1h} = 30$ | mm |

| | |
|---------------------------|---|
| Leading edge tip radius | $r_{1t} = 78 \text{ mm}$ |
| Impeller tip radius | $r_2 = 112 \text{ mm}$ |
| Exit blade height | $b_2 = 10.2 \text{ mm}$ |
| Blade angle LE tip | $\beta_{1t} = 26.5^\circ$ (from tangential) |
| Blade angle impeller exit | $\beta_2 = 52^\circ$ (from tangential) |
| Rotor tip speed | $u_2 = 586 \text{ m/s}$ |
| Relative Mach Number | |
| tip inlet | $M_{rel1t} = 1.3$ |
| Pressure Ratio | $\pi_{t12} = 6.1$ |
| Efficiency | $\eta_{st12} = 0.84$ |

The impeller design data are shown in Table 1. The main geometrical parameters including the blade angles at inlet and outlet are identical with those published by Pak, Krain and Hoffmann (1992). But the new rotor has a completely different blade geometry, thinner blades and less flow turning in the inducer inlet region to fit better the transonic inlet flow conditions. Additionally, it has splitter blades instead of full blades only, which reduces blade blockage and increases the achievable mass flow rate compared with a rotor without splitter blades.

The same measurement procedure as before was applied for the new impeller, i.e. performance as well as laser measurements were carried out. For determining the performance characteristic, total temperatures and total pressures were measured at compressor inlet and exit. The downstream total pressure was taken at the diffuser outlet at a radius ratio of $r_4/r_2=1.9$. Total temperatures were measured by 4 probes in the collector and an adiabatic diffuser flow was assumed. Additionally the static pressure rise throughout the stage was measured by a series of static pressure taps mounted in the shroud casing. At rotor exit 16 taps were circumferentially distributed to determine a reliable mean static pressure that was used to derive a rotor efficiency. Mass flow was measured with a venturi nozzle located in the suction pipe (Fig. 2). The rig was not insulated either during the performance or during the laser measurement tests. Tip clearances at inlet and exit were measured with pins of graphite. For the design speed these clearances were 0.5 mm at the inlet and 0.3 mm at the exit.

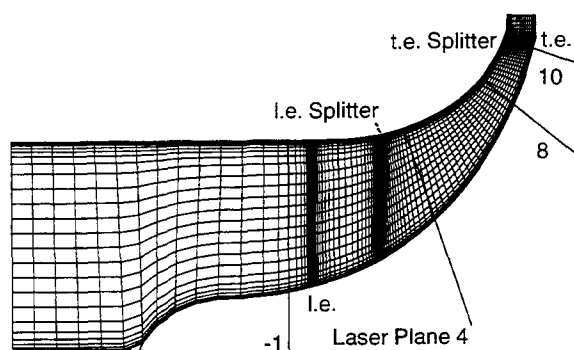


Fig. 3 Arrangement of laser measurement planes for the rotor and meridional input grid for 3D viscous calculations.

Figure 3 shows the arrangement of the laser measurement planes for the rotor and the input grid used for the 3D calculations. At each plane measurements were taken at 5 spanwise positions generally located at 10,30,50,70 and 90% channel height. A maximum of 16 measurement points are resolved in the pitchwise direction

in regions without blades. Inside the rotor this number is lower, because the blade region has to be excluded from measurements. For the high speed rotor under consideration 16 blade-to-blade measurement points are at present an upper technical limit for the laser system used for these investigations. Due to the splitter blades, measurements are subsequently performed in flow channels neighbouring a splitter blade. This procedure is necessary to take into account the different flow characteristics of adjacent flow channels. The splitters are located at mid-pitch of the long blade channels. Their geometry is the same as that of the long blades except in the vicinity of the leading edge where the splitters are thinner and rounded to limit the displacement effect and to avoid an undesirable high re-acceleration of the relative flow.

Performance Measurement Results

The maximum stage pressure ratio at design speed is 5.7:1 and the corresponding efficiency is 80%. Flow range from choke to surge $(\dot{m}_{choke} - \dot{m}_{surge}) / \dot{m}_{choke}$ is 19% (Fig. 4).

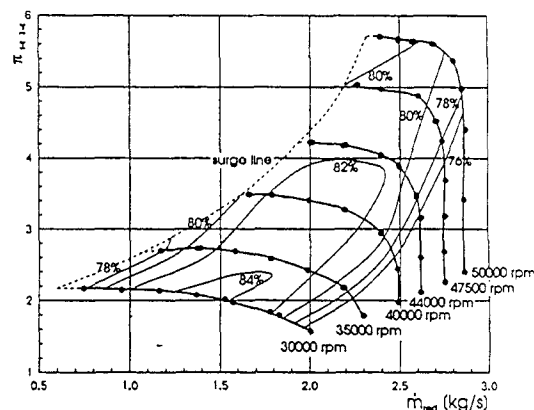


Fig. 4 Measured performance characteristic of the stage

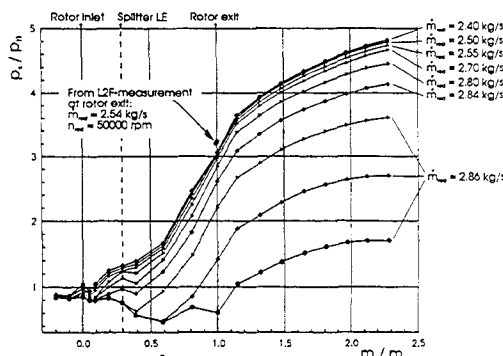


Fig. 5 Measured static pressure rise along the shroud contour and static pressure derived from laser measurements for design speed

Figure 5 shows the measured static pressure rise of the stage for nine mass flow rates at design speed. A very regular pressure rise occurs for mass flow rates close to the design point ($\dot{m}=2.55 \text{ Kg/s}$). The leading edge displacement effects of both the long and short blades are clearly reflected by a reduced pressure rise which is rising with rising mass flow especially at the splitter blade leading edge. In this plot the pressure at the rotor exit ($m/m_{ges}=1$)

is always a mean value of the 16 circumferentially distributed pressure taps. This pressure was taken to derive the rotor alone performance map shown in Fig. 6.

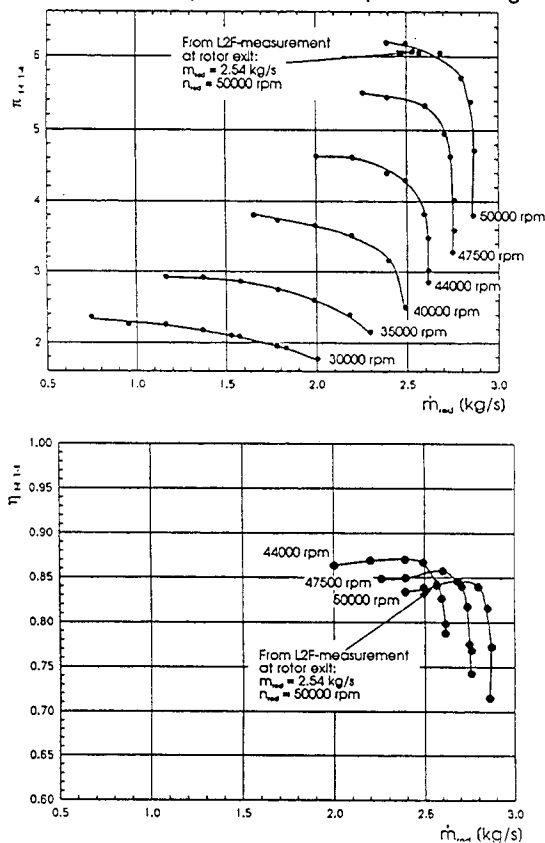


Fig. 6 Derived total pressure and total / total isentropic impeller efficiency. Design point performance additionally derived from laser data taken at impeller exit.

The total/total rotor pressure ratio and impeller efficiency were derived from the measured total temperature, mass flow and static pressure by using the continuity and Euler equation, which is a common procedure for rotor performance determination (Japikse, 1992, Yoshinaka, 1994, Simon et al., 1986, Colantuoni and Colella, 1992, Rodgers, 1990). Additionally, a blockage factor has to be taken into account which in the present case was assumed to be constant for all operating points (17%). This value and the measured shroud static pressure, taken as representative for the whole rotor exit area, influence the result. Therefore, it is important to evaluate rotor performance with a typical blockage factor. In the present case the 17% blockage was taken from an initial 3D flow calculation carried out for the design point with a rather coarse grid. With this blockage a 84% rotor efficiency was derived which is in fairly good agreement with the efficiency derived from the laser measurement data also shown in Fig. 6.

For the laser data the mean velocity was found by an integration across the exit area. The total temperature was derived from the absolute circumferential velocity component by applying the Euler equation. The total pressure

at rotor exit was obtained by adding the diffuser pressure loss to the measured pressure at the diffuser exit thus avoiding to take the measured shroud static pressure as representative for the whole exit region. Diffuser losses were calculated with the equation of mass conservation and the moment of momentum equation. The surface roughness was represented by a constant friction coefficient of $\lambda = 0.024$.

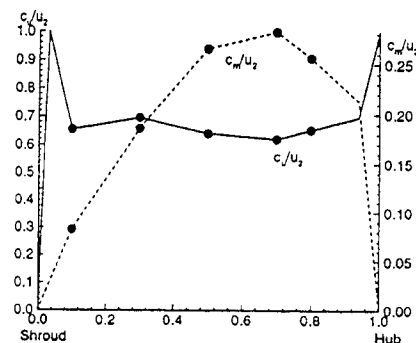


Fig. 7 Pitch mean velocity profiles taken from laser measurements and used for impeller efficiency determination

Figure 7 shows the pitch mean velocity profiles for the meridional and absolute circumferential velocity component used for the efficiency derivation. In the shroud region c_u is assumed to rise linearly from $c_u(z/b = 0.1)$ to $c_u = u_2$ at the blade tip and to fall to zero in the gap to meet the zero flow condition for the absolute velocity at the shroud. At the hub the velocity profiles are linearly extrapolated to the edge of the boundary layer, the location of which was estimated from the results of the 3D calculation. In the hub boundary layer region c_u rises to u_2 at the wall to satisfy the zero flow condition for the relative flow, because the hub wall of measurement plane 10 is still inside the rotating system as can be seen from Fig. 3. A rotor efficiency of 84.4% is derived by this procedure and the corresponding total temperature is 0.6 K higher than the mean total temperature measured with the probes. At the rotor exit a higher temperature than in the collector is to be expected because the rig was not insulated. The rotor efficiencies obtained from the conventional measurements (84%) and from the laser data (84.4%) are close to each other although they are derived in very different ways. The still existing uncertainties are mainly related to the near wall regions where boundary layer and/or wake flow is present. Laser measurements closer to the wall could reduce these uncertainties but it is not easy to take them because the rate of particles in the wake flow is generally low which makes the measurements very time consuming. Additionally, reflections of the laser beam will rise when going closer to the wall because the rotor under consideration has only an exit width of 10.2 mm (Table 1). The mean static and total pressures derived from the laser measurement data by assuming the velocity profiles shown in Fig. 7 are also given in Figs. 5 and 6. The agreement between both the laser and conventional measurements data is quite good.

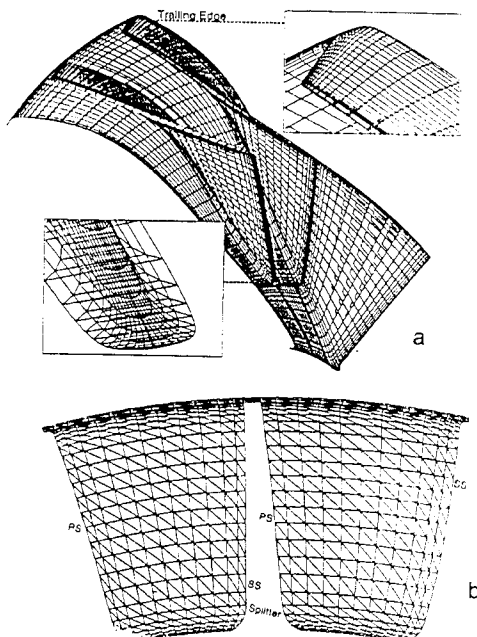


Fig. 8 a: Surface input grid for 3D viscous calculations,
b: Crossflow grid section with triangulated volumes.

Numerical Approach

The 3D-flow field of the splitter blade rotor has been calculated with the program system NEWT developed by Dawes (1991). This system has been integrated into FLOWSIM, (Hoffmann, 1990), and its pre- and post-processors have been modified to accept a special single H-type input grid block providing Cartesian surface coordinates (Fig. 8a) for

- the full- and for the splitter blades,
- the casing and hub, including the spinner geometry,
- blade tip clearances,
- blade fillet radii and
- rounded blade leading and trailing edges.

Initially the splitter blade grid lines are part of the interior flow field grid. The surface grid points of the splitter are then considered as solid wall points and coordinates inside are excluded via cell deletion. Thus, the splitter tip clearance gap is gridded and adequate for the physical gap, whereas the blades still have rounded tips to avoid singular grid points. The initial grid is also triangulated into an unstructured, adaptive one used by the flow solver (Fig. 8b). The input H-mesh has $29 \times 111 \times 25$ points in blade-to-blade, throughflow and hub-to-shroud direction respectively, and the corresponding unstructured mesh after cell deletion has 368544 tetrahedral control volumes with 68429 nodes for vertex storage of the primary variables p, v_x, v_t, v_r, p, k , and ϵ . Due to computer hardware restrictions, the implemented adaptive grid refinement of NEWT based on flow gradients has not yet been used, in order to limit the total number of grid points and to take the maximum amount of points to model more accurately leading- and trailing edges, tip clearances and blade fillet radii as shown in Fig. 8a. The tip clearance corresponds with the measured clearance and varies between 0.5 to 0.3 mm from leading- to trailing edge of the full blade. The blade fillets have constant radii of 2 mm. With respect to an impeller solution without splitter, (e.g. Pak et.al. 1992),

more than twice as many grid points are used for a splitted rotor with two separate flow passages to achieve approximately the same grid point density. An additional point density is needed in the throughflow direction near the leading edge of the splitter blade. Presently, this is supposed to give the best resolution for the restricted total number of points. Nevertheless, there are still not enough points to resolve sharp shock structures, and the boundary layer zones near the blade surfaces, especially in the rear part of the flow channel where local wall coordinates Y^+ of over 500 are present in the circumferential direction. The minimum Y^+ achieved is 29 near the hub leading edge and exceeds the implemented limit of $Y^+ = 10$. Thus the wall shear stress at the blade surfaces is computed from the log law equations, but not from the laminar sublayer.

The code solves the three dimensional, compressible, Reynolds-averaged Navier-Stokes equations with κ, ϵ -turbulence modelling on blocked, unstructured, adaptive grids. A four step Runge-Kutta time marching algorithm with residual smoothing updates the flow variables, which are assumed to vary piecewise linearly over the tetrahedral volume cell faces in between the vertices. The viscous stress terms at a node are derived from the surrounding cells by assuming piecewise constant derivatives of the viscous stresses. Artificial diffusion controls shock capture and solution decoupling. Surface nodes, that could interfere with the physical viscous terms, are protected from additional smoothing. At the inflow boundary spatial distributions of total pressure, total temperature and swirl velocity are held constant during the time step iteration process. The static pressure is fixed downstream at the hub and the pressure variation across the exit annulus is calculated via the equation of radial equilibrium. Solid surfaces are assumed to be adiabatic.

Comparison of Experimental and Numerical Results

Laser-2-Focus measurements and numerical flow calculations were carried out for the design point (Table 1). The laser measurements are triggered circumferentially point-by-point on surfaces of revolution with respect to the absolute frame of reference. Based on that data, distributions of relative flow motion are derived for presentation on cross flow planes traversed by the laser beam. The numerical solution output is given on scattered unstructured spatial coordinates but within the boundaries of the previously mentioned structured input grid. Based on this input grid, 3D-surfaces similar to the laser measurement surfaces have been splined. The computed flow variables have then been interpolated onto grid points of the generated laser surfaces. By this technique, numerical- and experimental Mach number distributions for the laser planes -1, 4, 8 and 10 of Fig. 3, are compared in Figs. 9-12. The experimental relative Mach number was computed from measured velocity and inlet temperature by applying the equation of constant rothalpy. The mass flow achieved by the 3D-calculation was 0.04 kg/s lower than that of the measurements at design speed. A block-type velocity distribution is generated by the inlet bell-mouth of the test rig (Fig. 2). This type of velocity pattern was also taken as input for the 3D-calculations. The general grid

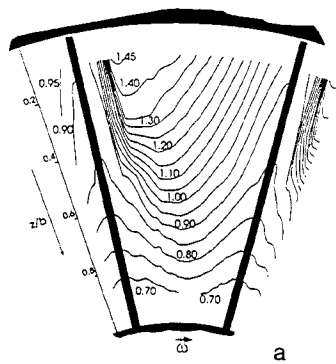
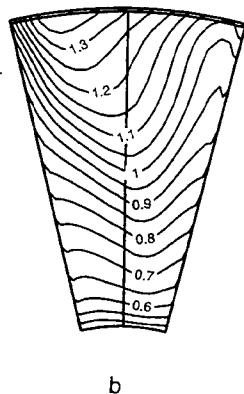


Fig. 9 Plane -1



b

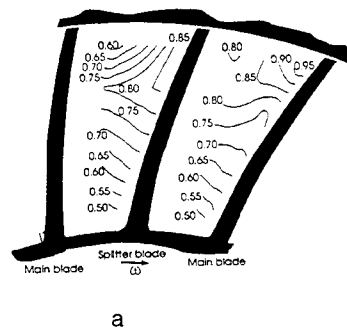
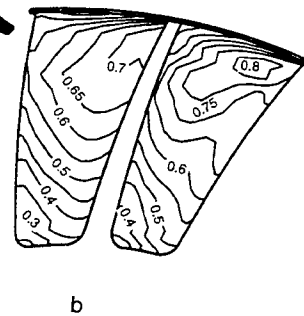


Fig. 10 Plane 4



b

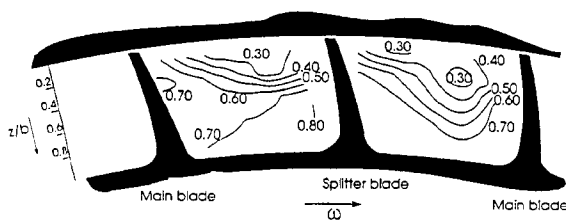
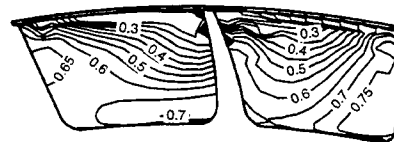


Fig. 11 Plane 8

a



b

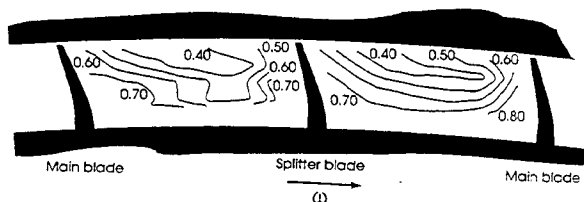
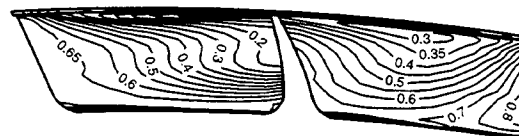


Fig.12 Plane 10

a



b

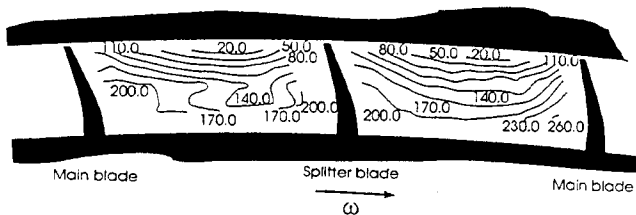
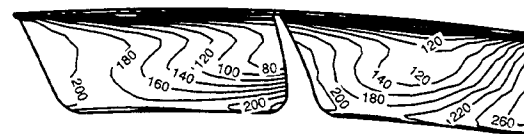


Fig.13 Plane 10

a



b

Fig. 9 - 12: Comparison of laser measured and calculated relative Mach numbers in planes -1 to 10 (Fig. 3).

Fig. 13: Comparison of laser measured and calculated meridional velocities in plane 10 (Fig. 3).

a: Measurement b: Calculation

$n = 50000 \text{ rpm}$, $\dot{m} = 2.55 \text{ Kg/s}$

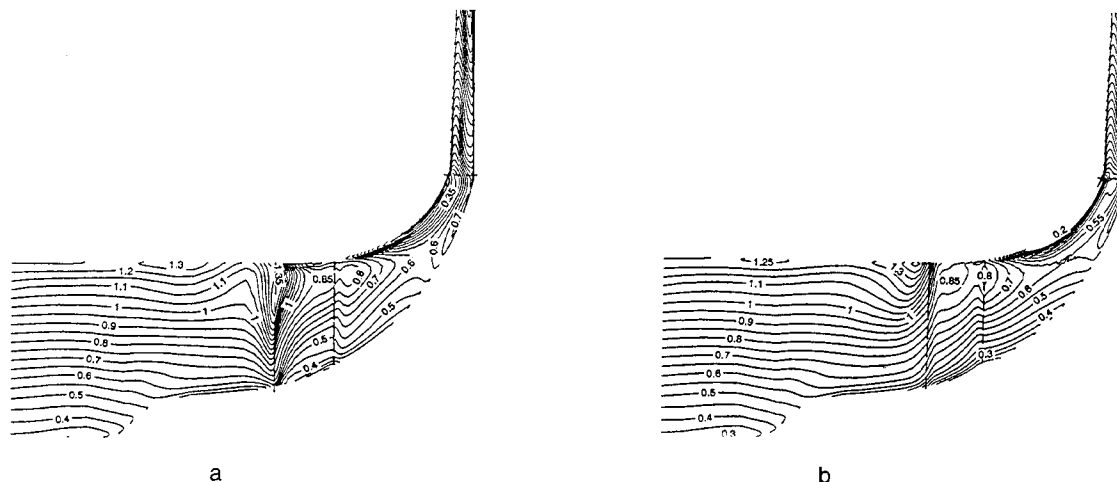


Fig. 14 Calculated relative Mach numbers at mid-pitch of adjacent flow channels.
a: Flow channel A (compare Fig. 15) b: Flow channel B (compare Fig. 15)

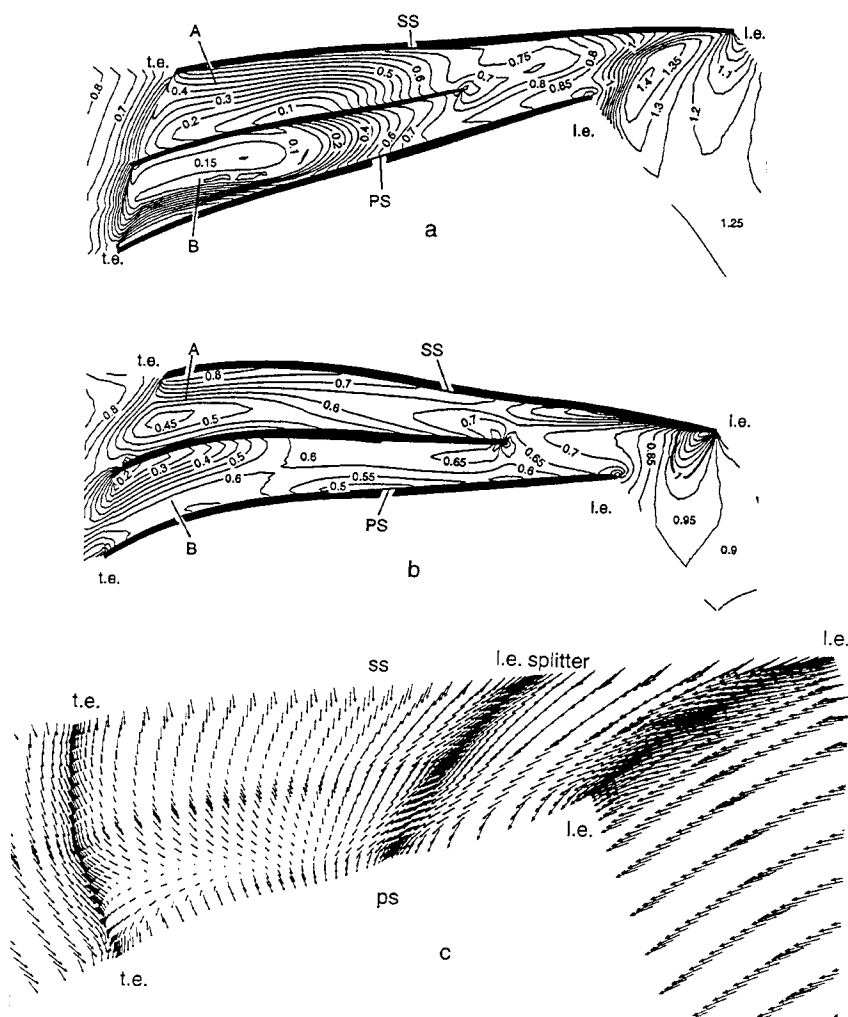
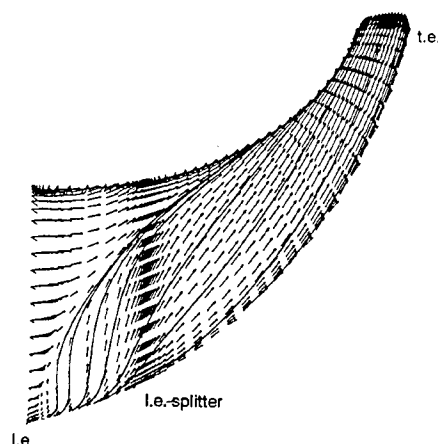
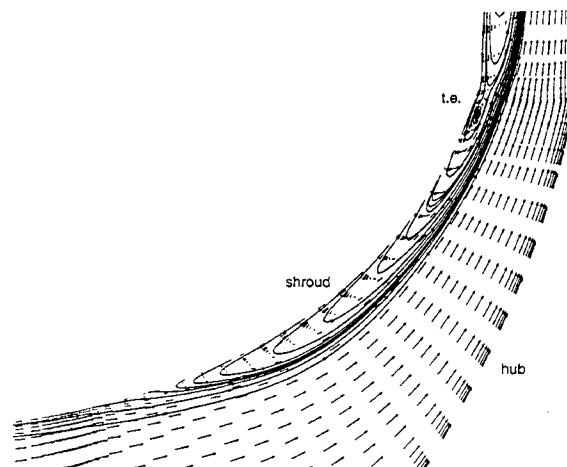


Fig. 15 Calculated blade-to-blade distributions for adjacent flow channels.
a: Mach number close to the shroud b: Mach number close to mid-span
c: Vectors of relative velocity in the tip clearance gap



a: Close to the suction side



b: Mid pitch channel B (compare Fig 15a)

Fig. 16 Calculated relative velocity vectors and flow traces

coarseness, is mainly believed to cause the existing discrepancies between the computed and experimental results. Hence, the shock passing laser plane -1 ahead of the impeller blade leading edge could not be resolved as sharply as found by measurement (Figs. 9 and 15). Within the bladed part of the flow channel, a lack of near wall flow blockage and hence secondary flow can be seen for all the laser planes. The calculated peak Mach numbers are not as high as those derived from experiment. Major differences between CFD- and experimental results occur near the splitter suction side (left flank of the splitter blade) in Figs. 11-13. The meridional velocities are negative in the region near the shroud and indicate reverse flow (Fig. 16b).

Additional mid-pitch hub-to-tip and blade-to-blade 3D-surfaces are presented to give more insight into the flow structure of the rotor under consideration. Figures 14 a,b are plots of relative Mach number in the splitter passages A and B. Passage A is bounded by the full blade suction side and the splitters' pressure side, see Fig. 15. The x-axis points in the direction of the rotor axis. The flow decelerates from supersonic to subsonic over a leading edge shock surface that extends from half span to the shroud. Downstream the flow is subsonic everywhere. The rotor's high curvature and its high rotational speed generate strong secondary flows and hence streamwise vorticity. The near wall motion of low momentum fluid for the suction side of the blade can be seen from Fig. 16a. The stream traces show that, between the leading edge locations of blade and splitter, the fluid of the hub boundary layer is turned into the radial direction. This flow is dominated by centrifugal forces. The rapid change to radial flow is further amplified by the transmission through the shock surface upstream to the leftmost streamline. Fluid that reaches the shroud joins the tip clearance flow. The primary direction of fluid close to the stationary shroud is from suction- to pressure side due to the tip clearance flow that follows the pressure gradient between pressure and suction side and due to the inertial forces, Fig. 15c. The streamline deviation due to Coriolis forces supports this near wall relative flow

behaviour. The low momentum fluid accumulates in the shroud region of the bladed passages and is shed into the main stream. This behaviour is shown by the relative flow velocity vectors plotted in a blade-to-blade surface close to the shroud (Fig. 15c). Hence, a typical jet/wake pattern is formed. The formation of the wake starts far downstream of the supersonic flow area. Thus, it can be concluded from this numerical solution, that the wake region is not generated via shock boundary layer interaction. The streamline pattern in the mid-pitch meridional plane of channel B (Fig. 16b) indicates a separation zone which extends into the diffuser. It is amplified by the sharp casing bend close to the trailing edge and increases the meridional blockage of the diffuser flow. A corresponding figure for channel A is not shown, but its separation zone is much smaller. Both reverse flow regions of the low-momentum fluid zones degenerate to very thin layers and vanish further downstream. The reverse flow region is relatively thin with respect to the hub-to-tip length, but it builds up a meridional local blockage of nearly 25% within each of the two passages at the rotor exit. There were not any measurements in the diffuser, which could further help clarify the reasons for this separation. As known from former investigations, (Krain and Hoffmann, 1989 b), the shroud contour curvature significantly influences the wake development inside the rotor. If the compressor were to be run with this vaneless diffuser, the CFD results could be taken to guide modifications of the impeller shroud and diffuser geometry so as to reduce the wake and reverse flow. But as mentioned previously, this diffuser will be replaced by a vaned type, which will alter the situation.

Conclusions

Performance and laser measurements as well as 3D viscous calculations were carried out for a high speed splitter blade rotor having transonic inlet flow conditions. The supersonic flow covers about 50% span at the rotor leading edge. From the theoretical results it is found that the maximum local relative Mach number is limited for this

rotor to 1.4 (Fig. 15). A distinct shock induced separation has not been resolved by the computations and the measurement data available for planes -1 and 4 are not sufficient to confirm a separation from the experimental point of view. Additional measurements are necessary in the tip region of the rotor to resolve the shock structure in more detail. On the theoretical side calculations using a finer input grid or the implemented adaptive grid refinement technique need to be carried out to get a further improvement in boundary wall flow resolution. This will also contribute to a deeper understanding of the flow characteristics in regions of shock surfaces. A jet/wake type flow pattern, very similar to that known from subsonic rotors, is also present in this rotor operating with transonic inlet flow conditions. Laser measurements and CFD results indicate low velocity regions close to the shroud downstream of the splitter blade leading edge, building up a significant blockage at the rotor exit.

Acknowledgement

The project is sponsored by Forschungsvereinigung Verbrennungskraftmaschinen e.V., a consortium of German and Swiss turbine manufacturers. The new rotor was designed in co-operation with German and Swiss industry with major support of Mr. Eisenlohr from BMW/RR who is chairman of the group. The authors would like to thank W. Weimann, H. Fischer, D. Dörrenhaus and H. Hasler for preparing the tests.

References

- Balje, O.E., 1981, "Turbomachines", John Wiley & Sons, New York, Chichester, Brisbane, Toronto
- Casey, M.V., Dalbert, P., Roth, P., 1990, "The Use of 3D Viscous Flow Calculations in the Design and Analysis of Industrial Centrifugal Compressors", ASME Paper 90-GT-2
- Chriss, R. M., Hathaway, M.D., Wood, J.R., 1994, "Experimental and Computational Results from the NASA Lewis Low-Speed Centrifugal Impeller at Design and Part Flow Conditions", ASME Paper 94-GT-213
- Colantuoni, S., Colella, A., 1992, "Aerodesign and Performance Analysis of a Radial Transonic Impeller for a 9:1 Pressure Ratio Compressor", ASME Paper 92-GT-183
- Dalbert, P., Gyarmathy, G., Sebestyen, A., 1993, "Flow Phenomena in a Diffuser of a Centrifugal Stage", ASME Paper 93-GT-53
- Dawes, W.N., 1991, "The Simulation of Three-Dimensional Viscous Flow in Turbomachinery Geometries Using a Solution Adaptive Unstructured Mesh Methodology", ASME Paper 91-GT-124
- Dawes, W.N., 1994, "A Simulation of the Unsteady Interaction of a Centrifugal Impeller with its Vaned Diffuser: Flow Analysis", ASME Paper 94-GT-105
- Eckardt, D., 1976, "Detailed Flow Investigations within a High Speed Centrifugal Compressor Impeller", ASME Journ. of Fluids Eng., Vol. 98, No. 3, 390-402
- Eisenlohr, G., Chladek, H., 1993, "Thermal Tip Clearance Control for Centrifugal Compressor of an APU Engine", ASME Paper 93-GT-137
- Hah, C., Krain, H., 1990, "Secondary Flows and Vortex Motion in a High Efficiency Backswept Impeller at Design and Off-Design Conditions", ASME Journ. of Turbom., Vol. 112, pp.7-13, Jan. 1990
- Hathaway, M. D., Chriss, R. M., Wood, J.R., Strazisar, A., J., 1992, "Experimental and Computational Investigation of the NASA Low-Speed Centrifugal Compressor Flow Field", ASME Journ. of Turbom., Vol. 115, No. 3, 527-542.
- Hoffmann, W., 1990, "A Computer Program System for the Analysis of 3-d Steady Flows in Turbomachinery", (in German). DLR-FB90-18
- Howard, J.H.G., Ashrafizaadeh, M., 1994, "A Numerical Investigation of Blade Lean Angle Effects on Flow in a Centrifugal Impeller", ASME Paper 94-GT-149
- Japikse, D., 1992, Course Notes on: "Centrifugal Compressor Design and Performance", Concepts ETI, Inc., Norwich, Vermont
- Josuhn-Kadner, B., 1994, "Flow Field and Performance of a Centrifugal Compressor Rotor with Tandem Blades of Adjustable Geometry", ASME Paper 94-GT-13
- Krain, H., 1981, "A Study on Centrifugal Impeller and Diffuser Flow", Trans. of the ASME, Journ. of Eng. for Power, Vol. 103, Oct. 1981, pp. 688-697
- Krain, H., Hoffmann, W., 1989 a, "Verification of an Impeller Design by Laser Measurements and 3D-Viscous Flow Calculations", ASME Paper 89-GT-159.
- Krain, H., Hoffmann, W., 1989 b, "Centrifugal Impeller Geometry and its Influence on Secondary Flows", AGARD-CP-469, Secondary Flows in Turbomachines
- Moore, J., Moore, J.G., 1990, "A Prediction of 3D-Viscous Flow and Performance of the NASA Low-Speed Centrifugal Compressor", ASME Paper 90-GT-234
- Pak, H., Krain, H., Hoffmann, B., 1992, "Flow Field Analysis of a High Pressure Ratio Centrifugal Compressor", AGARD CP 537, pp 17.1-17.12
- Pinarbasi, A., Johnson, M. W., 1994, "Off Design Flow Measurements in a Centrifugal Compressor Vaneless Diffuser", ASME Paper 94-GT-42
- Rodgers, C., 1982, "The Performance of Centrifugal Compressor Channel Diffusers", ASME Paper 82-GT-10
- Rodgers, C., 1990, "Centrifugal Compressor Inlet Guide Vanes for Increased Surge Margin", ASME Paper 90-GT-158
- Rodgers, C., 1991, "The Efficiencies of Single Stage Centrifugal Compressors for Aircraft Applications", ASME Paper 91-GT-77
- Schodl, R., 1989, "Measurement Techniques in Aerodynamics", VKI Lecture Series 1989- 05
- Simon, H., Wallmann, T., Mönk, T., 1986, "Improvements in Performance Characteristics of Single Stage and Multistage Centrifugal Compressors by Simultaneous Adjustments of Inlet Guide Vanes and Diffuser Vanes", ASME Paper 86-GT-127
- Ubaldi, M., Zunino, P., Barigozzi, G., Cattanei, A., 1994, "An Experimental Investigation of Stator Induced Unsteadiness on Centrifugal Impeller Outflow", ASME Paper 94-GT-5
- Yoshinaka, T., 1994, "Aerodynamic Design and Performance Characteristics of the Centrifugal Compressor", UTC Technical Education and Training